



An automated surface determination approach for computed tomography

Xiuyuan Yang ^{a,b}, Wenjuan Sun ^a, Claudiu L. Giusca ^{b,*}

^a Surface Engineering and Precision Centre, Cranfield University, Cranfield, Bedfordshire, MK430AL, UK

^b Engineering Department, National Physical Laboratory, Hampton Road, Teddington, TW11 0LW, UK



ARTICLE INFO

Keywords:

X-ray computed tomography
Surface determination
Watershed
Non-destructive dimensional inspection

ABSTRACT

Surface determination is a critical image processing step in X-ray Computed Tomography that uses algorithms based on local thresholding methods, such as Canny and Steinbess, to detect the surface of metallic components with intricate designs and complex topographies. In most of the cases, these algorithms require trial-and-error tests to optimise the threshold operation, leading to unreliable and, at times, erroneous inspection results. This paper demonstrates the ability of marker-controlled watershed algorithm to automate the surface determination process and to maintain its robustness in the presence of beam hardening and complex topographies, outperforming the current commercial and non-commercial software implementations.

1. Introduction

The automotive and aerospace sectors and, recently, additive manufacturing (AM) increasingly employ X-ray computed tomography (XCT) as a nondestructive technique (NDT) to inspect the internal and external features (geometry, topography and defects) of modern components, which in some cases are impossible to assess using conventional measurement techniques [1–3].

XCT instruments capture a series of radiographic projections of an object/component at multiple angular positions that are subsequently used to reconstruct a three-dimensional (3D) representation of that object, as shown in Fig. 1-A. The 3D representation associated with the object consists of a cluster of voxels with different grey values compared to the intensity of the voxels corresponding to the background. In the example shown in Fig. 1-A, dark grey shade voxels represent the background and the light grey shade voxels represent the object (or foreground). The geometrical measurements are derived from the surface of the object, which has to be established from the 3D representation of the object.

From the initial projections to the final geometrical evaluation, there are various factors that affect the measurement results, such as instrument alignment, focus spot stability, user-defined scanning parameters, material, geometry, photon-material interaction, orientation of the component, reconstruction and surface determination (SD) algorithm [4,5]. SD plays a critical role in the XCT measuring model as it impacts on the effect of the other factors on the geometrical measurements, i.e., their associated sensitivity coefficients [6]. The role of SD algorithms is

to find, often with sub-voxel resolution, the boundary situated in the transition area between the background and the object (the white line in Fig. 1-B) that is associated with the surface of the object. Hence, any errors introduced by SD algorithms lead to significant errors in the measurement [5,7–16].

XCT inspection of porosity [13,17–19], surface roughness [3,13,20–24] and dimensional conformity [12,13,25–29] require accurate spatial location of the surface, therefore, the reliability of SD algorithm has gained extensive attention. Lifton [19] and Carvalho [2] pointed out that unproper SD algorithm can result in unwanted pores to be detected due to the presence of noise. Townsend [30,31] compared the impact of different SD algorithms on surface texture analysis using XCT and found that for the same volume reconstructed, *Sa* deviation under iterative method within VGStudio MAX 2.2, a proprietary software most used in practice, was 20% off compared to global threshold method (Otsu). Lifton [32] showed that in the case of AM components the global and local SD methods can lead to 25 μm difference in diameter measurement. Whereas, the bi-directional distance measurements of multi-material samples can be affected by errors as large as 12.04 μm and 126.5 μm when the SD uses Canny and local thresholds algorithms, respectively [8].

Despite the importance of the SD process, commercial software does not provide sufficient transparency – i.e., SD is regarded as a black box, impeding the development of complete uncertainty models. To understand the impact of SD algorithms, an example of a real measurement of two closely positioned spheres and the associated SD process performed with VGStudio MAX version 3.2.5 in “advanced mode” is shown in

* Corresponding author.

E-mail address: c.giusca@cranfield.ac.uk (C.L. Giusca).

Fig. 2. VGStudio, like Steinbess algorithm [33], computes global surface at the first stage, and find the vertex location with maximal gradient magnitude along each point of global surface normal, subject to search distance setting. Under the influence of beam hardening, ‘streak’ artefacts [34] occur causing severe deviations of the surfaces (inset B and C for 2D case and inset D for 3D case). The operators can increase the search distance to minimize this effect, but this can lead to unrepeatable results and will not mitigate the effect of beam hardening on the roughness measurements. Most importantly, rough SD should consider low spatial resolution (or high spatial frequency). By increasing the search distance, the norm of search vector can exceed the spatial resolution of desired rough surface, hence not detecting small spatial surface wavelengths.

The SD algorithms used for XCT measurement can be classed as: (i) *global threshold methods* [14] and (ii) *local adaptive threshold methods* [15].

i. *Global threshold methods*: Otsu [14] and ISO50 [16] are the most common global threshold methods used to separate the background from the object. Both methods, represented pictorially in Fig. 3, are histogram-based algorithms that return a single grey threshold value situated between the background and object. Otsu's threshold value (T_{Otsu}) relies on the minimization of the between-class variance for the background and foreground [14], whereas ISO50 returns the threshold value (T_{ISO50}) at the midpoint between peaks of the object and background histograms (T1 and T2 in Fig. 3). The voxels with the grey values higher than the threshold value are classified as foreground, i.e. the object, and the rest as background. However, both methods are sensitive to the image artefacts. For example, Otsu method is affected by beam hardening [5,35] and scattering that can lead to measurement errors as large as 9% [36]. Meanwhile, a single threshold value may not be able to determine the surface accurately (low adaptation) in some areas of the 3D representation of the object, due to the voxels' intensity variation along the boundary between the foreground and the background [5].

ii. *Local adaptive threshold methods*: In contrast to the global methods, local adaptive algorithms calculate the maximum local gradient [13]. Examples include Canny [9], Steinbess algorithm [33] and Heinzel method [37].

Firstly, the Canny algorithm [9] uses the non-maximum suppression technique to find all local maxima, which then are labelled as

pre-determined edge. In a following step, two thresholds, low and high, are set to select the desired edge from the pre-determined edge. To begin with, the pixels of the pre-determined edge that have an intensity greater than the high threshold value will be marked as the edge (hard edge). Then, the pre-determined edge pixels with an intensity smaller than the low threshold will be discarded. The pre-determined edge pixels between the high and low threshold values are marked as ‘soft edge’ in the following step. Lastly, the soft edge connecting with the hard edge will be marked as the hard edge; otherwise, those soft edges will be discarded. However, relevant thresholds have to be appropriately chosen to avoid broken-up and noisy surfaces [9]. For example, inappropriate threshold selection could result in omitting edges, as shown in Fig. 4. The threshold for selecting the inner and outer cylinder surface can differ.

The Steinbess algorithm [33] is equivalent to the ‘local adaptive threshold’ method used in VGStudio. The Steinbess algorithm computes the global threshold surfaces (initial surface), then generates the grey value profiles along the normal vectors of the initial surface and calculates the maximum gradient values, which make final surface points. The Steinbess algorithm can be affected by noise [37] and rough surfaces.

The Heinzel [37,38] algorithm applies an anisotropic diffusion filter, a gradient filter, and a watershed filter sequentially. The anisotropic diffusion filter reduces noise while preserving the specific image features, such as edges [39]. The gradient filter is employed to calculate the gradient data at each voxel by computing the directional derivative. The watershed filter segments the reconstructed data into groups based on the regional maximum gradient model to generate the edge data (for more details, see section 2). ‘Flooding level’ is controlled manually to avoid over-segmentation. However, the manual selection of the flooding level makes the Heinzel algorithm ‘less robust’.

Local adaptive methods have been proven to be more accurate than the global thresholding method [5,12,28,37,40]. However, some of the local adaptive methods, such as the Canny algorithm, are sensitive to noise [28]. Thus, most local adaptive algorithms employ various smoothing filters to reduce the noise effect [5,9,32,37,41,42] and to obtain smooth surfaces, which also leads to errors associated with the operator. Korner and Staude et al. [41,42] applied and compared several smoothing filters (e.g., 2D and 3D median filters implanted within Fiji,

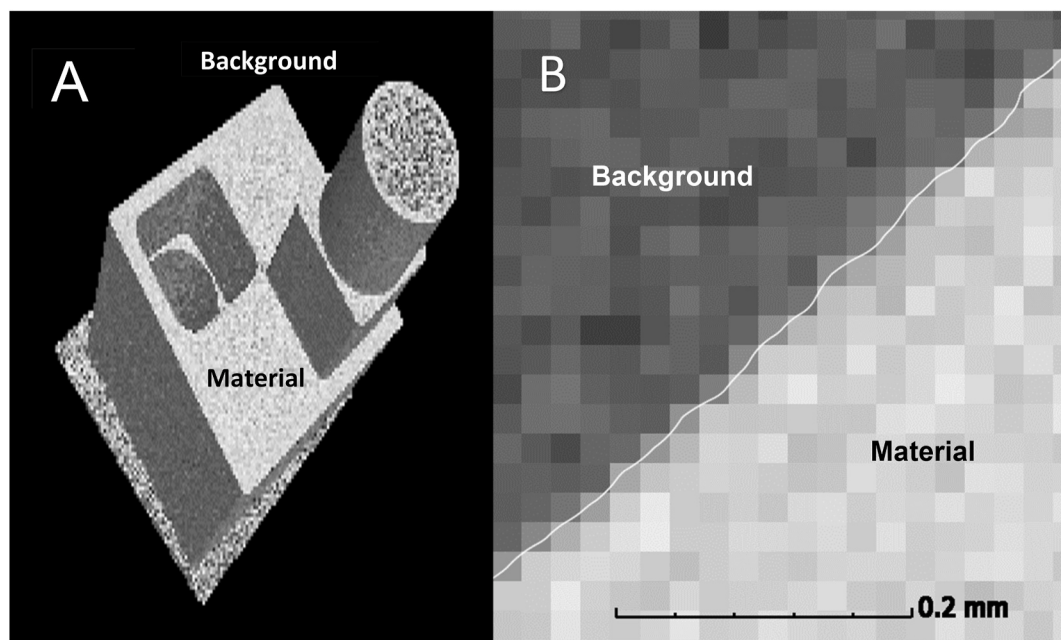


Fig. 1. A: The reconstruction of the National Physical Laboratory's (NPL) AM measurement standard; B: The cross section of the sample showing the position of the determined edge relative to the background and the object.

VGStudio and CT Pro) using the calotte cube reference (material: titanium alloy Ti-6Al-4V) to increase the signal-to-noise ratio and highlighted a depreciation in the resolution while applying a smoothing filter.

The evidence reviewed here highlights the need for the development of SD algorithms that are robust in the presence of noise and beam hardening artefacts. In response to these issues, the marker-control watershed (MCW) algorithm reduces over-segmentation (see section 2 for more details) and has been used successfully in the medical field [43–45] to extract the features of interest, often organs, and evaluate their dimensions. So far, there are only a few studies related to the MCW algorithm applied in the XCT inspection of components with higher density, hence requiring higher penetration energy, leading to additional errors, such as beam hardening. Moreover, previous studies [22, 46] mainly focused on using watershed to segment surface features,

including freeform surfaces. However, the ability of using watershed to detect the surface from raw volume data, especially detecting inner features and surface textures, has not been thoroughly explored.

This paper reports the 2D implementation of the MCW algorithm in XCT measurement to determine the surface of smooth and rough components. The work has been established with both simulation and experimental data considered. Section 2 introduces the workflow of MCW algorithm in detail; Section 3 proposes the methodology and methods behind the simulation experiments used to validate and compare the algorithms using a CAD reference sample; Section 4 presents summary results and analysis of the effects of beam hardening and noise on the MCW surface; Section 5 is a discussion of the effect of markers selection and interpolation ratio. The last section, Section 6, provides summaries and conclusions, and signposts the future work.

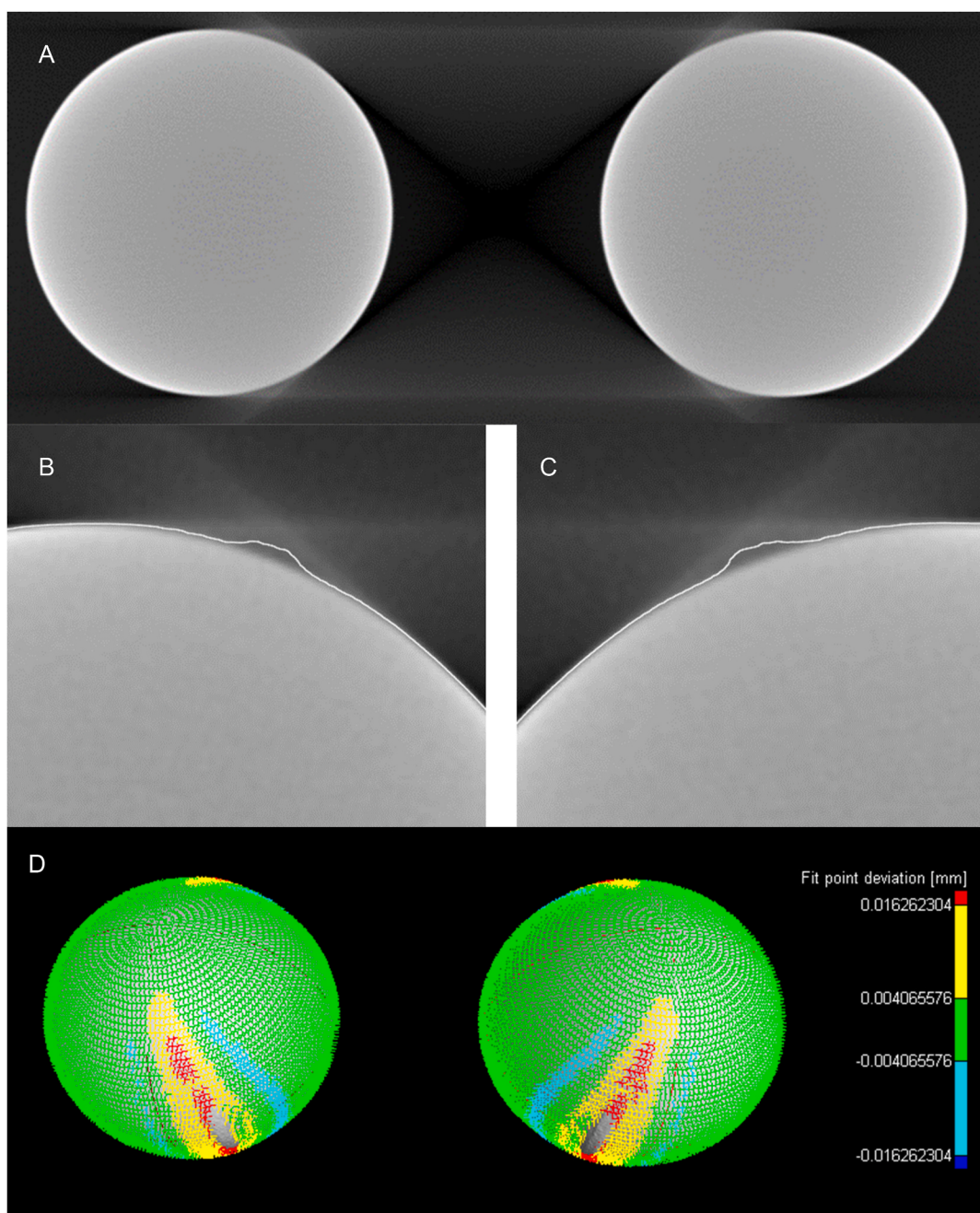


Fig. 2. Measurement results of two spheres standard using the advanced threshold algorithm in VGStudio Max 3.2.5, 'Streak' artefacts are present on side of the spheres.

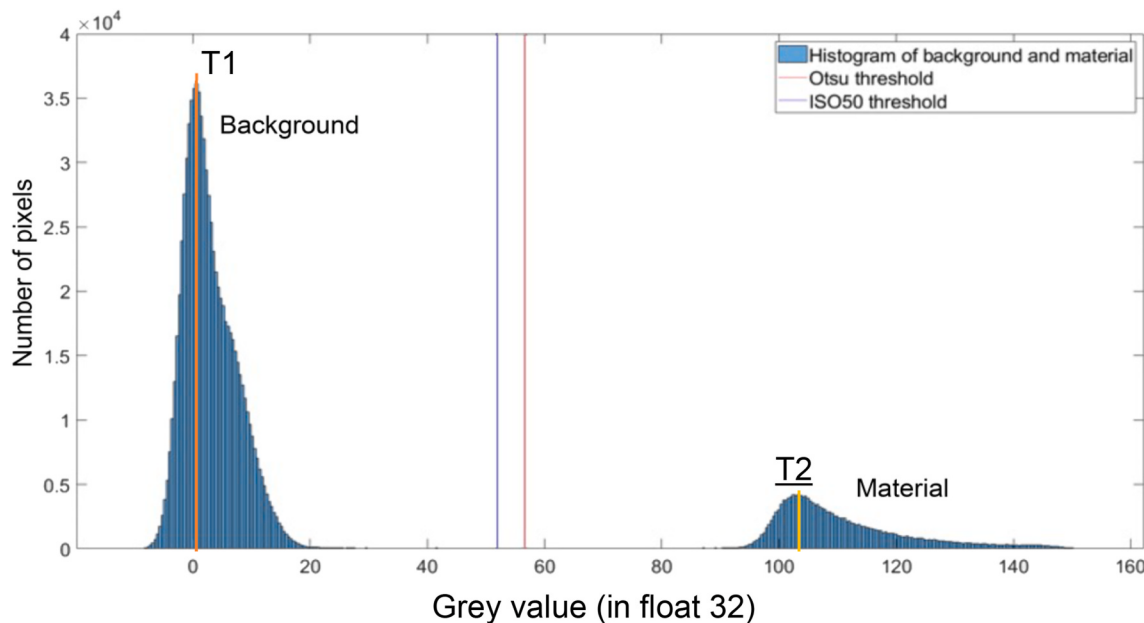


Fig. 3. The histogram of a reconstructed XCT image with a total number of pixels N, showing the calculation of Otsu threshold and ISO50 threshold. The grey value is shown in ‘float 32’ format.

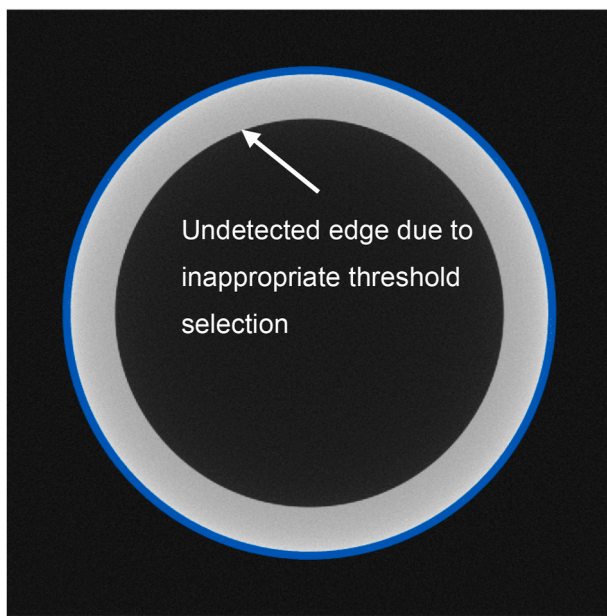


Fig. 4. Canny edge detection with inappropriate threshold selection.

2. MCW algorithm implementation

A significant drawback of conventional watershed-based algorithms is over-segmentation, which appears in the presence of a large number of minima in the gradient image [37,38]. An example of image over-segmentation is shown in Fig. 5, where the large amount of local catchment basins is caused by noise. Beucher [47] developed the MCW algorithm by introducing marker labels and geodesic transformation, and it successfully reduced the over-segmentation.

In Step 1, the original image is used to compute the foreground and background markers automatically. At Step 2, a high-resolution gradient image is obtained from the original image that is subsequently filtered at Step 3 using the geodesic transformation. The foreground and background markers define the image region on which the geodesic

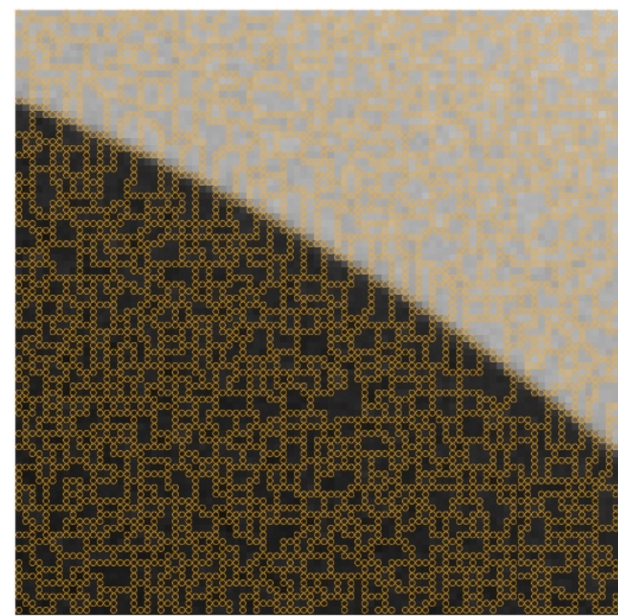


Fig. 5. Over-segmentation after watershed without any pre-processing.

transformation is not applied. Finally, at Step 4, the watershed transformation takes place on the filtered gradient image to identify the surface points. These steps are detailed below.

Step 1. Foreground (material) and background (air) markers

The marker selection was performed automatically using an opening-closing reconstruction algorithm, as described in Ref. [48]. An initial threshold is calculated based on ISO50 [12], then a closing operator and erosion morphology transformation [47] is applied on the regions above and below the initial threshold to establish the foreground and background marker, respectively. The closing operator eliminates the smaller pores within the marker region. The erosion transformation shrinks the marker region to assure that markers do not overlap the edges and eliminates the regions outside the desired foreground marker. Both

closing operator and erosion transformation include a structuring element in the shape of disk with a radius r .

With reference to Fig. 6, the value of 1 is assigned to the pixels of the original image (A) whose positions are within the material region of the foreground marker image (the green region in B), and 0 is assigned to the remaining pixels of the foreground marker image (black region in B). Conversely, the values of pixels that belong to the background region are set to 1 in the background marker image (yellow region in C) and 0 for the remaining pixels. The size of the markers was reduced using an erosion algorithm so that the markers do not cover the pixels surrounding the edges.

For comparison, the manual selections of the foreground and background markers were shown to demonstrate their roles in the geodesic transformation and their influence on the determined watershed edge. As shown in Fig. 7, the foreground and background markers can be chosen manually with various sizes and positions.

Step 2. Interpolation and image gradient transformation.

Spline interpolation is applied to the 2D reconstructed images to obtain an image with sub-pixel resolution that preserves the characteristics of the original image [49]. Here, we define p as the ratio between the length of the side of the pixel after interpolation and before interpolation.

Subsequently, the Sobel gradient operator [50] was applied over the interpolated reconstructed slice image and the result is shown in Fig. 8-A. In Fig. 8-B and C, foreground and background markers are superimposed on the gradient image respectively.

Step 3. Geodesic transformation over gradient of reconstructed slice

To overcome the over-segmentation problem, a geodesic transformation [47] was applied to the gradient image produced at step 2 to reduce the number of minima [47] as a result of noise. The geodesic transformation process is illustrated in Fig. 9 (2D), Fig. 10 and Fig. 11 (3D). The black dash box marks the size and position of the marker; blue solid and green dash lines indicate the original plot (f) and geodesic transferred plot (f'), respectively. All the data points within the black dashed regions in Fig. 9 were set to negative infinite, indicating the regions of minima.

Starting from point A, which is the point of intersection between the boundary of the left-hand side marker and the line f , the geodesic transformation draws the line f' to point B, which has the same altitude as point A but is on the opposite side of the valley. The line f' takes the same values as f until the original plot reaches the peak point C. From point C, the line f' maintains the same value until it reaches point D at the opposite side of the valley. Concurrently, the same process is started from the background marker and the moves towards the left. The line f' started from foreground marker boundary goes up until point G in the graph, where joins the plot started from the background marker. Thus,

the line f' contains only the regional minima whose locations overlap with markers' location. All other regional minima in the line f disappear, i.e. the valleys E and F will not be seen in the final line f' .

In the 2D range, the figures in the next two pages described the comparison of the 2D gradient image before and after geodesic transformation in topographic relief. The figures in the second page are the zoom-in of the section in the first page labelled by red rectangle. Markers, or the local minima, are labelled to describe that after geodesic transformation, the regions labelled by markers are set as negative infinite. According to the zoomed in figures, before geodesic transformation, there are numerical local minima within the topographic relief. After geodesic transformation, local minima are reduced to the region labelled by markers in previous step, while all other pre-local minima regions are replaced by the plains. In other words, in topographic relief, every droplet in a random location within a catchment basin (e.g., the green dashed region in the figure on next page) related to the local minima can flow to the local minima region without the need of climbing up a hill.

Step 4. Watershed transformation

The watershed transformation [51] is applied on the gradient image (f') to separate the object from the background and extract the coordinates of point cloud corresponding to the edge data. The basic watershed algorithm, including the concept of geodesic influence zone, immersion process and related mathematical expressions are detailed in Ref. [52]. The immersion process simulates the flooding of the topographic relief, the water being allowed to run in from the regions corresponding to the local topographical minima. As the catchment basins submerge, water from adjacent catchment basins meet together at the ridge. Here, dams are built to prevent the exchange of the water between the adjacent catchment basins. The dams form the watershed edge. When the whole topographic relief is submerged, the watershed transformation segments the image into partitions composed of geodesic influence zones associated with a single catchment basin. Applying watershed on f' would not cause the over-segmentation problem. The peak point of the line f' can be precisely detected due to the elimination of all other regional catchment basins. As shown in Fig. 12, when viewing any image as a topographical map, the set of points where the water will flow down under gravity to a catchment basin will belong to that basin. In contrast, the watershed lines are given by a set of points that do not belong exclusively to any catchment basin. In this way, the whole topographical map is segmented into different regions, and the watershed lines denote the determined surface.

Minimum M is a series of connected pixels with the altitude level h . Lower levels cannot be reached without climbing (see minima M in Fig. 12). The catchment basin C belonging to M , $C(M)$, includes the set of pixels from which a drop of water flows down and eventually reaches M (see catchment basin $C(M)$ in Fig. 12).

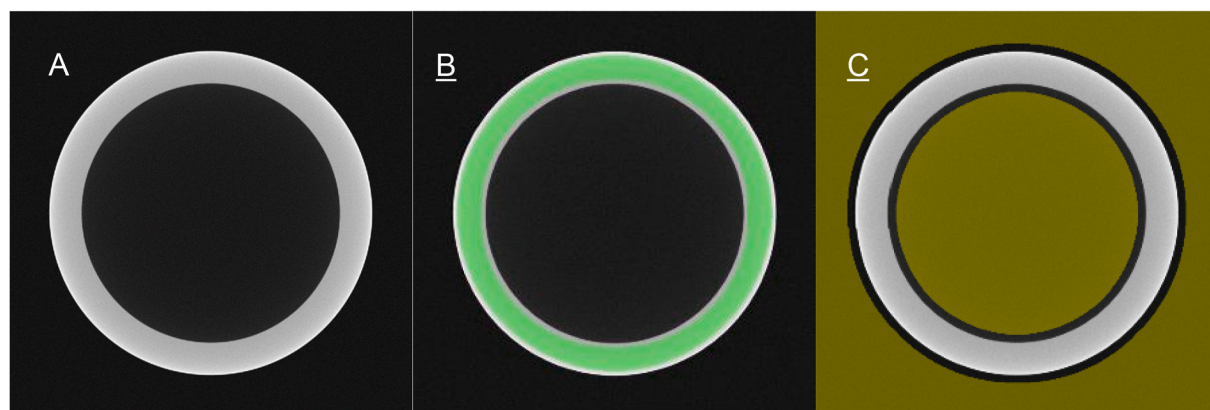


Fig. 6. A. Original reconstructed image; B: Foreground marker (higher grey values); C: Background marker (lower grey values) by automatic selection.

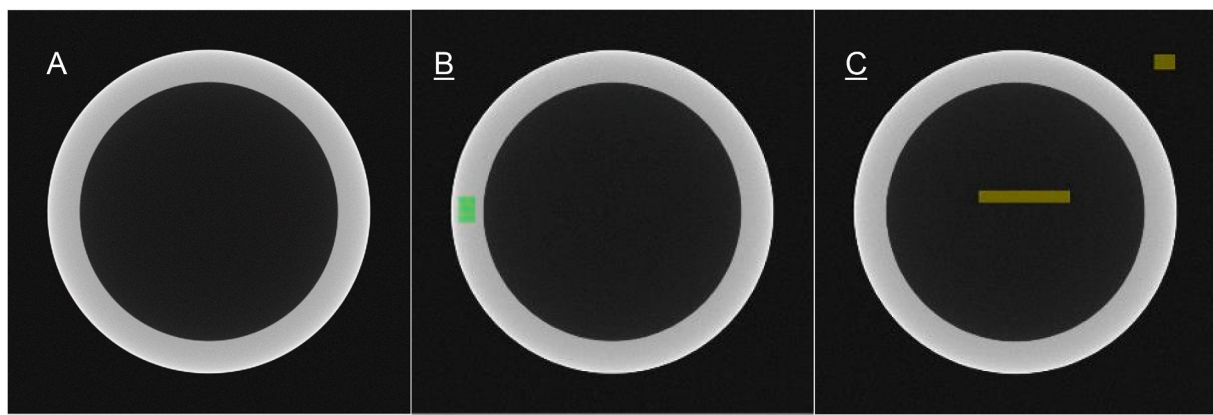


Fig. 7. A. Original reconstructed image; B: Foreground marker (higher grey values); C: Background marker (lower grey values) by manual selection.

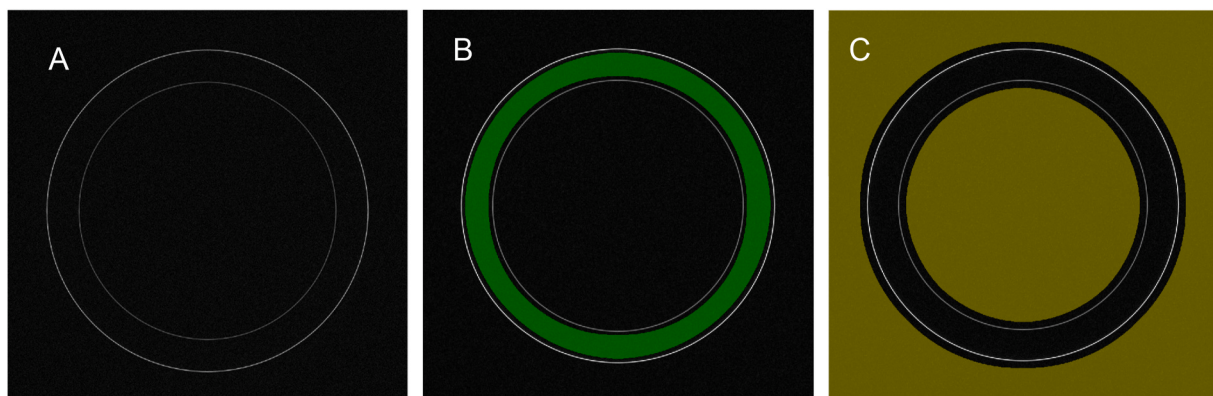


Fig. 8. A: The gradient image after applying Sobel operator convolution. B: Gradient image combined with foreground marker. C: Gradient image combined with background marker. Markers originate from Step 1.

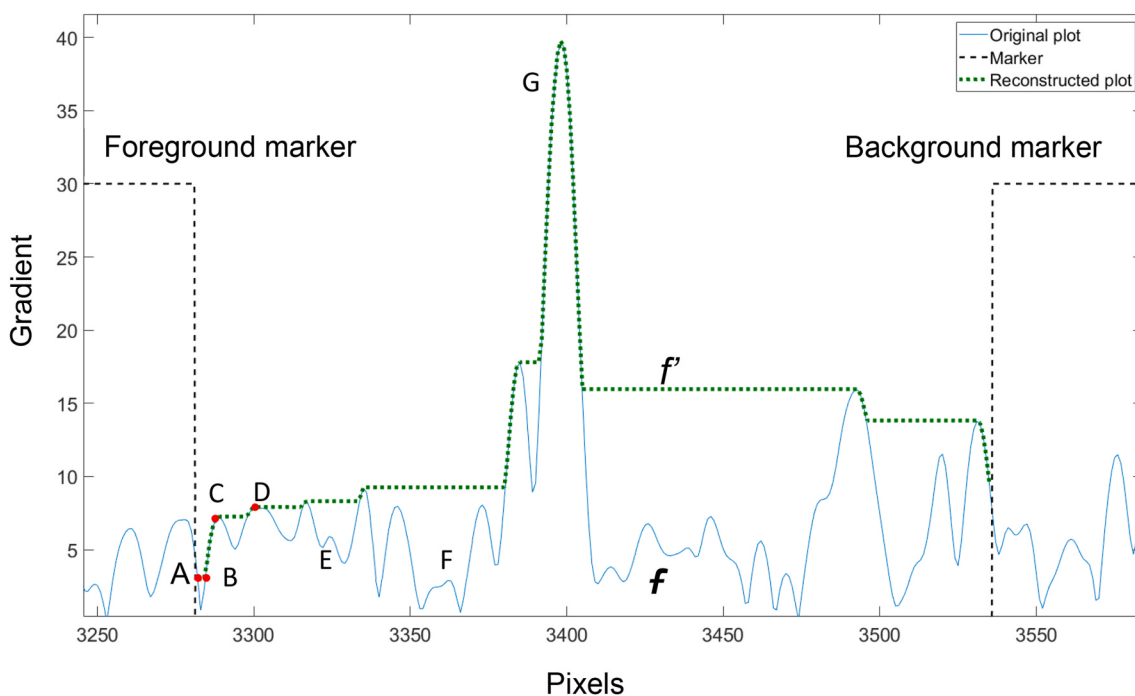
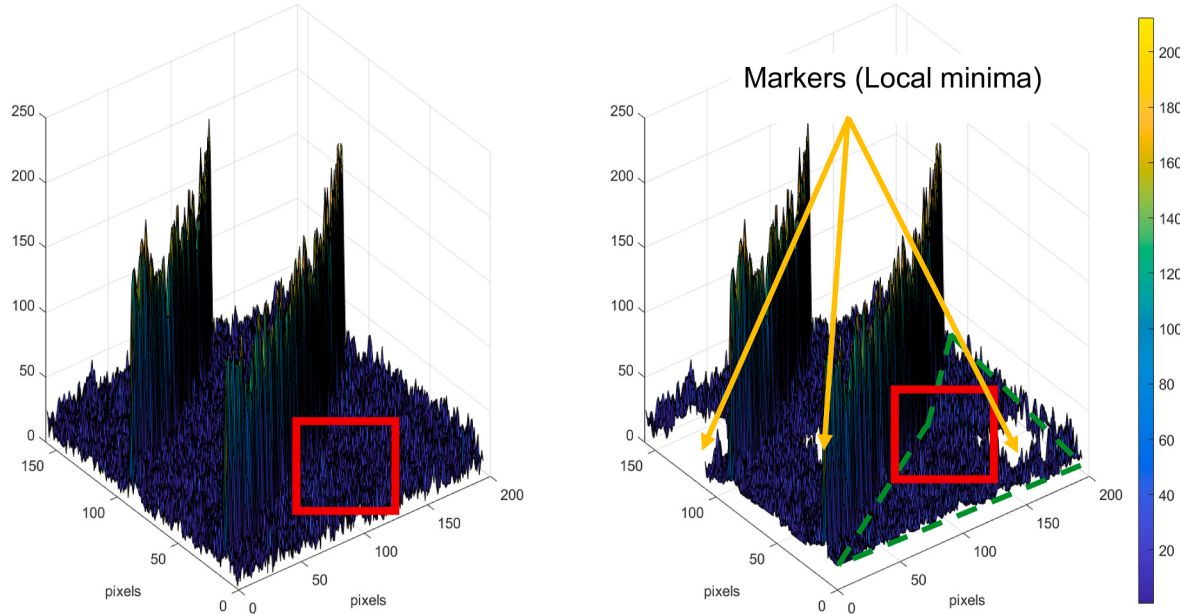
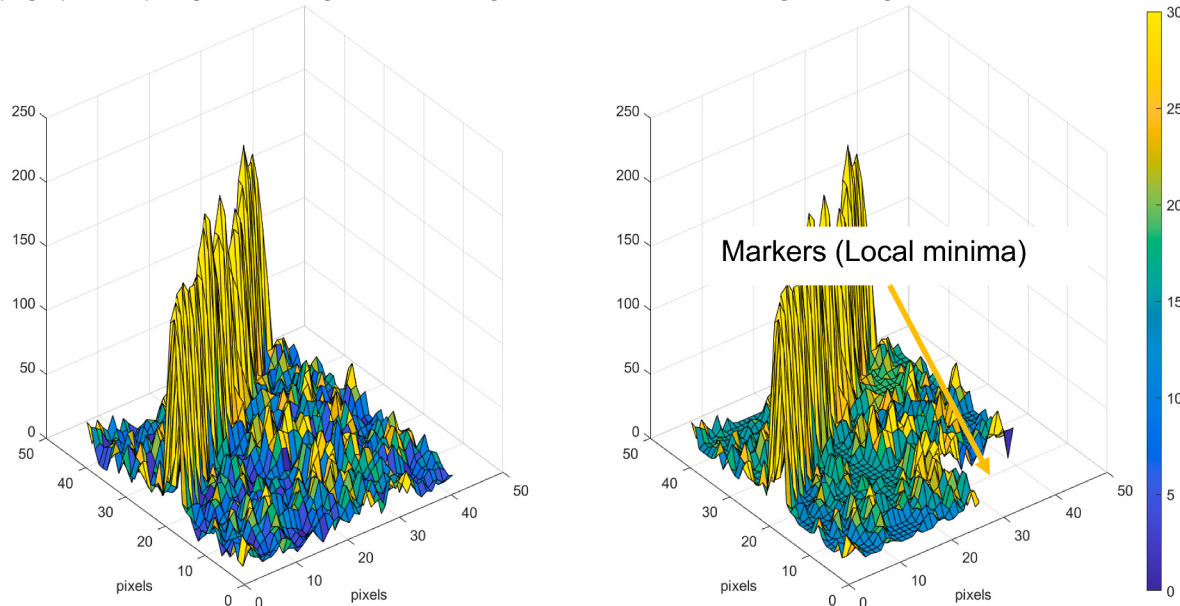


Fig. 9. The geodesic transformation. The rectangular black dash box indicates the position and size of markers; blue solid plot indicates the original plot (f); green dotted plot (f') indicates the plot after geodesic transformation from f . (For interpretation of the references to colour in this figure legend, the reader is referred to the Web version of this article.)

Topographic map of gradient image. Left: before geodesic transformation; Right: After geodesic transformation

**Fig. 10.** Topographic map of gradient image: Left: before geodesic transformation; Right: After geodesic transformation.

Topographic map of gradient image. Left: before geodesic transformation; Right: After geodesic transformation

**Fig. 11.** The zoomed in topographic map of gradient image. The zoom in region is labelled in red rectangular in **Fig. 10**. (For interpretation of the references to colour in this figure legend, the reader is referred to the Web version of this article.)

3. Methodology

3.1. Reference sample and XCT simulation conditions

A 3D CAD model of a reference sample was used for the MCW benchmarking. Similar to previous studies that used calibrated objects [10,12,16,32,53], the design of the reference sample, presented in Fig. 13, consists of cylinders with the following characteristics:

- The outer cylinder radius of the smaller tube is equal to the inner cylinder radius of the larger tube, allowing comparison of the results for inner and outer features,

- the reference sample has a simple structure with symmetry around the vertical axis [54], and
- the material considered is aluminium.

The radii of each cylinder were determined at three positions (L1 to L3 and H1 to H3 in Fig. 13 B). The least square circle fitting method (Pratt method) [55] was used here.

This study used simulated XCT projections to evaluate the quality of the MCW algorithm and investigate the influence of various parameters. The XCT projections of the reference sample were simulated using a commercial software package aRTist 2.10.4 [56], which is based on ray-tracing method. The parameters of simulations listed in Table 1 are

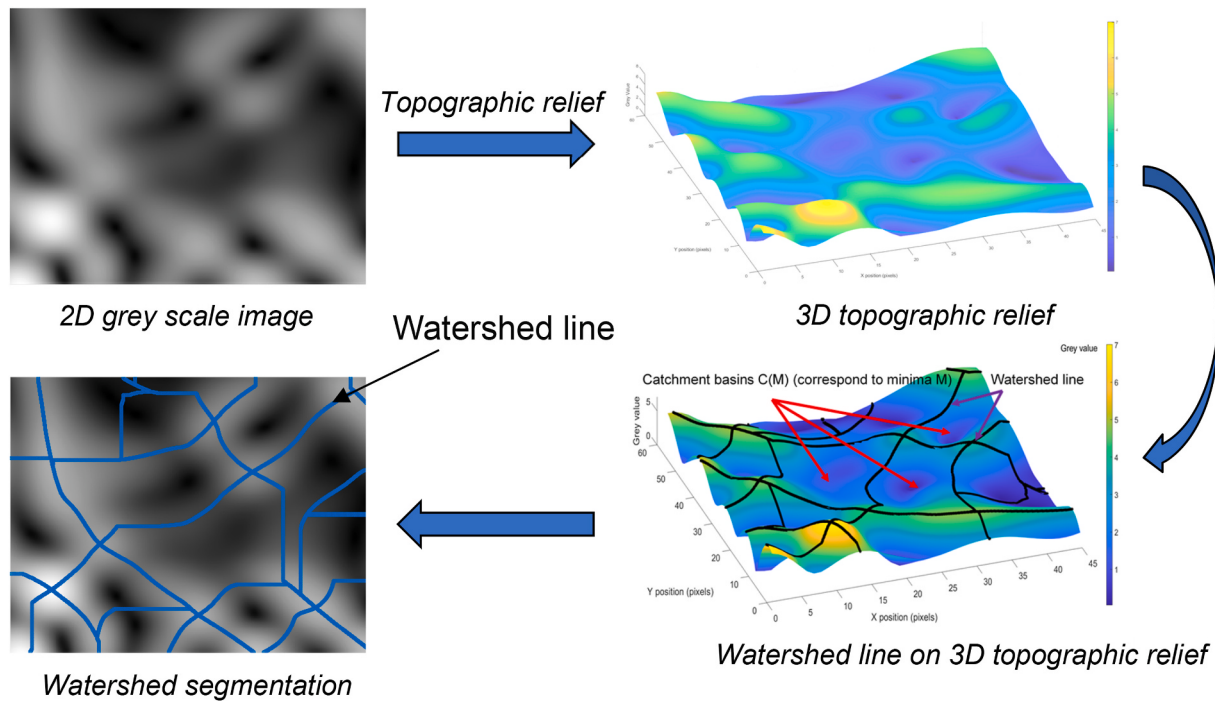


Fig. 12. The diagram of the watershed segmentation process.

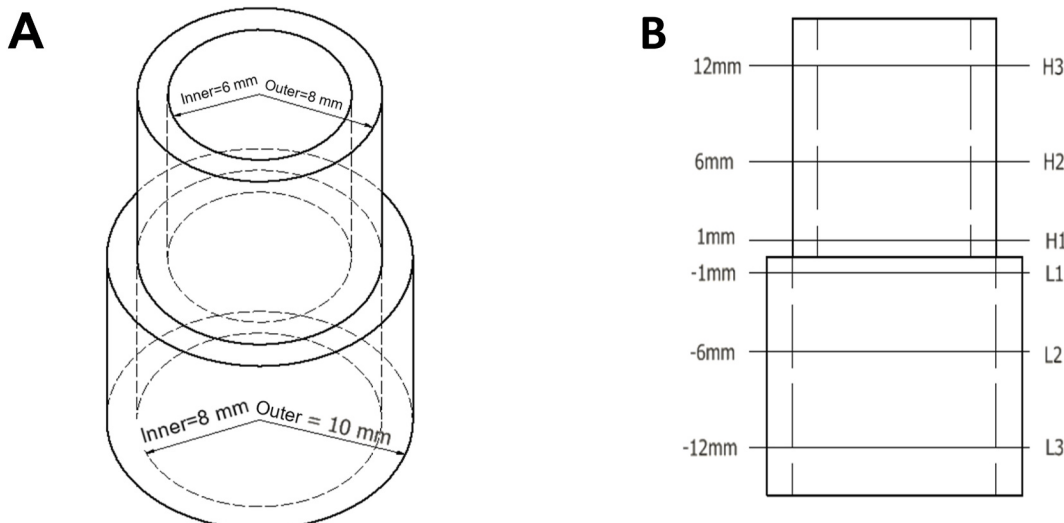


Fig. 13. The overlapped tube reference sample: A. The drawing of radius of the CAD model B. Positions of 2D cross-section images considered along the vertical axis.

Table 1
Settings of simulation.

Voltage kV	Current μA	Number of projections	Magnification	Voxel size in μm	Multi-sampling
100	80	3143	8	25	3x3

commonly used in experimental work.

This study considered three sets of XCT simulations:

- Set 1: Monochromatic scan, *i.e.* without beam hardening and noise, etc.
- Set 2: A scan that accounted for beam hardening (polychromatic) effects without noise.
- Set 3: A scan that included the effects of both beam hardening and noise.

- Set 3: A scan that included the effects of both beam hardening and noise.

To mimic experimental results, the signal-to-noise ratio of a real system has been studied. The XCT system considered is a Nikon XT H 225 M cone beam system with a reflection target. The noise of the instrument has been evaluated, ranging between (75–150) kV and (60–100) μA , respectively. For 100 kV and 80 μA , the value of the SNR is approximately 155, which was subsequently used in simulations. It should be noted that this work did not consider scattering, as there is only slight scatter effect when X-ray penetrates aluminium.

3.2. Data processing

The simulation projections were reconstructed with Feldkamp, Davis

and Kless (FDK) algorithm [57] using CT Pro 3D version 5.4. For polychromatic simulation data, beam hardening correction was neglected as it can cause reduction of signal-to-noise ratio [58]. For sub-pixel resolution purpose, a spline interpolation algorithm was used to subdivide the voxel in three interpolation ratios 0.1, 0.2, 0.5. $p = 1$ denotes that no interpolation was conducted before applying the watershed. In the case of $p = 0.1$, each pixel was subdivided into 10×10 pixels using spline interpolation. The MCW implementation was implemented in MATLAB 2019b. While applying MCW algorithm, the structuring element for closing and erosion transformation was set as a disk with a radius of 20 pixels.

For comparison with the MCW algorithm, a MATLAB [48] function that implements the Canny algorithm was used in this work to segment the 2D cross-section of reconstructed data. The *threshold* input variable is a two-element vector [*low*, *high*] which takes values in the range of [0,1] and is used to establish the final edges. The *low* value provides the threshold below which all edges are discarded (weak edge) while the *high* value is the threshold above which all edges are preserved (strong edge). To ensure that all defined (strong) edges are connected, the edges situated between these two threshold values are labelled as strong edges if they are connected with a strong edge pixel and discarded otherwise. The *low* and *high* values are set by the operator using a trial-and-error method, as there are still no robust methods for the selection of the threshold input variable.

4. Summary of results

4.1. Benchmarking - monochromatic and polychromatic (beam hardening) case

The results of benchmarking test are shown in Fig. 14. The errors (ε) were displayed in pixels to show the error relative to voxel size. For monochromatic (simulation set 1, no beam hardening) and polychromatic (simulation set 2, with beam hardening) cases, at $p = 0.1$. The errors are calculated as the difference between the measured radius and the nominal radius defined in the CAD model.

The monochromatic case shows that there is little difference between the outputs of the MCW and Canny algorithms, which demonstrates that both algorithms are equally effective in ideal measurement conditions. It is important to note that the error of the radii fitted to the inner and

outer cylinders have different sign and magnitude, approximately +0.4% and -1.1% of pixels, respectively.

Compared with monochromatic results, the beam hardening effect had a marginal effect on the radius of the inner cylinders (less than 0.02% of the error), which corroborates with the work of Lifton [32] and Villarraga-Gómez [13]. However, for the outer cylinders, the difference between monochromatic and polychromatic measurement results are as large as 3.3% of pixels, which suggests that during the reconstruction process the beam hardening effect significantly altered the value of the pixels surrounding the edge of outer cylinders. It appears that the grey value can vary with different material thickness, but this assumption needs further attention.

The results for polychromatic case, i.e. beam hardening, agrees with Villarraga-Gómez [13] findings, which concluded that the beam hardening shifts the surface point clouds of the external surfaces toward the background side. This explains the differences between radii calculations of the inner and outer cylinders in different XCT measurement conditions, that is to say, monochromatic and polychromatic.

4.2. Noise effect on the MCW

Fig. 15 allows comparison of the surface point cloud distribution without (left) and with (right) noise at $p = 0.1$. The solid red line represents the surface based on nominal data. In both cases, the MCW algorithm generated closed surfaces with no scattered points. In the absence of noise (Fig. 15-C) the surface's point cloud remains within $\pm 10\%$ of the pixel away from the nominal data, whereas in the presence of noise (Fig. 15-D) the point cloud errors from the nominal ranges within $\pm 20\%$ of the pixel size. This suggests that noise affects the gradient image, which consequently alters local maximum grey values detected by the watershed algorithm. The geodesic transformation eliminates most of the local minima in the gradient image and reduces over-segmentation, however, the magnitude and x and y position of the gradient maxima could still be affected by noise.

The error chart presented in Fig. 16 indicates that the mean radii of the inner cylinder measured with and without noise do not deviate by more than 0.5% of pixels from their nominal size and the mean radius error of the outer cylinder is approximately +2.5% of pixels. The standard deviation associated with the radius measurement of the inner cylinders of the tube is larger than the results on the outer cylinder.

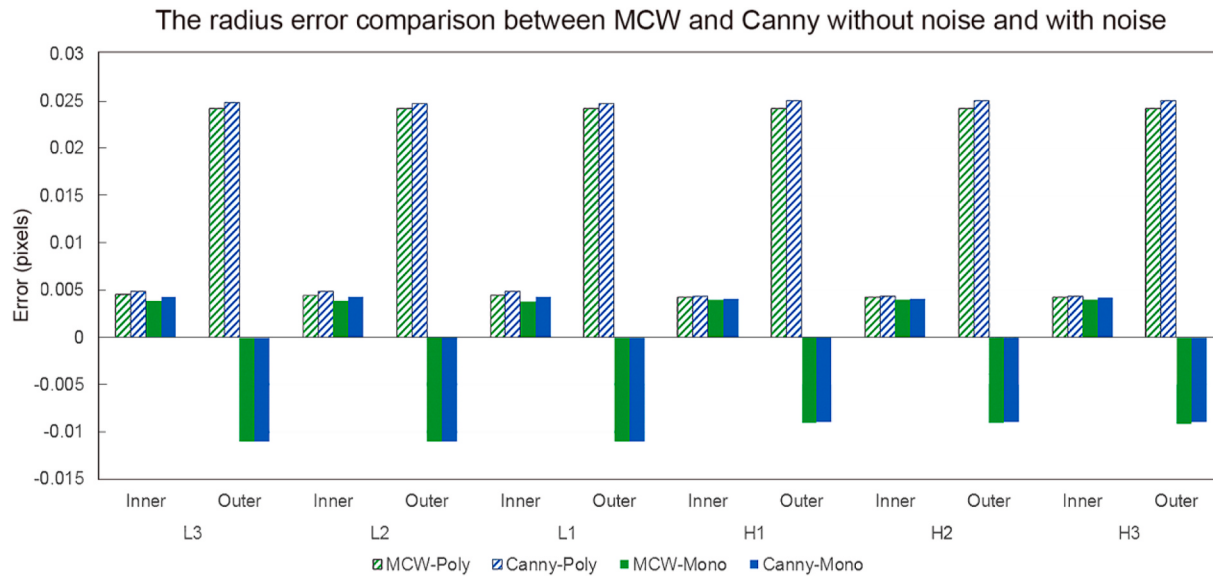


Fig. 14. The error of radius for simulation set 1 (benchmark, monochromatic, no beam hardening) and simulation set 2 (polychromatic, beam hardening), noise factor = 0, Interpolation ratio $p = 0.1$, mean radius value and error bars are based on five individual MCW and Canny applications over five slices within the range of ± 10 layers around each benchmark (L3-H3) layers.

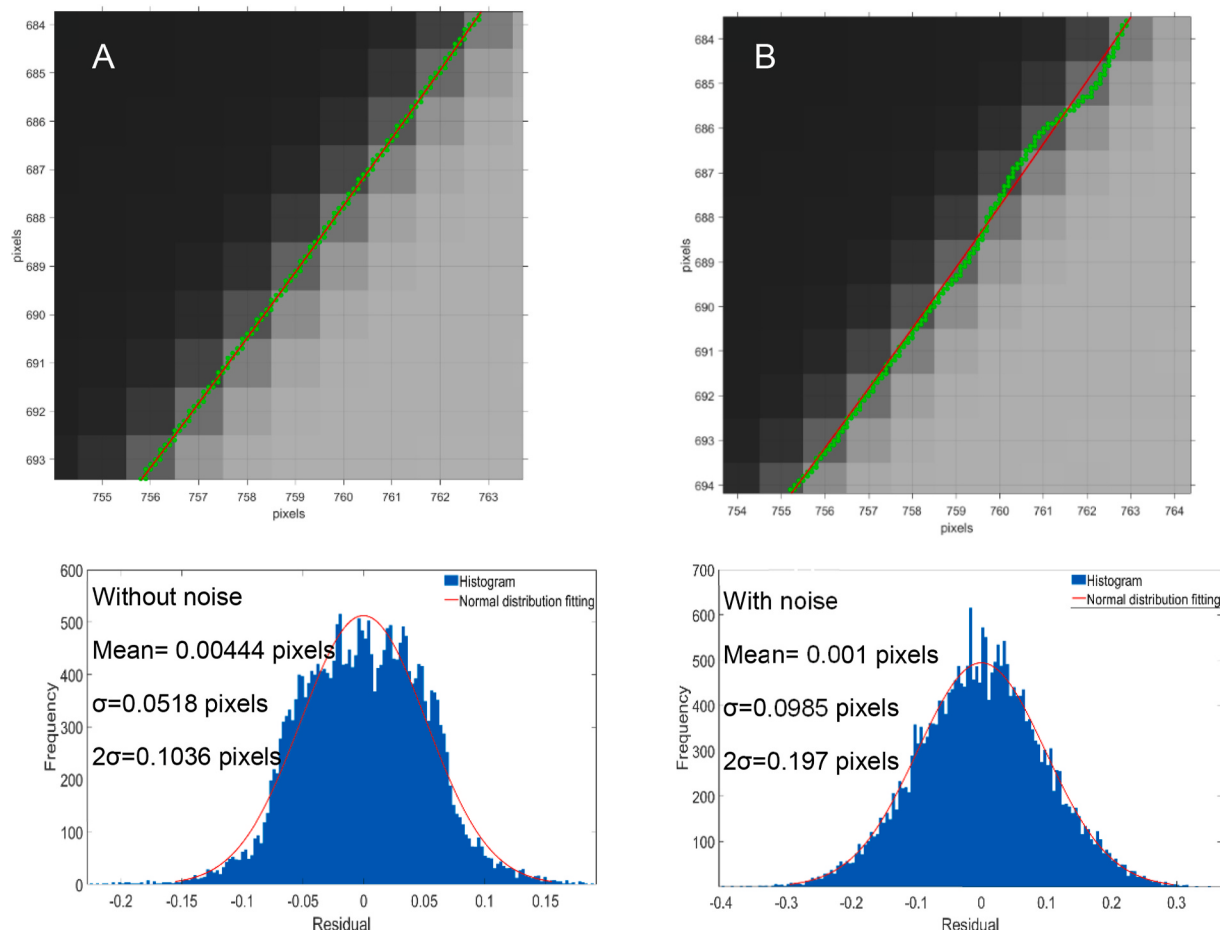


Fig. 15. Surface point clouds and residual histogram determined by MCW under simulation set 2: Polychromatic. Left column: Without noise. Right column: with noise. Slice height index: L2, Interpolation ratio $p = 0.1$.

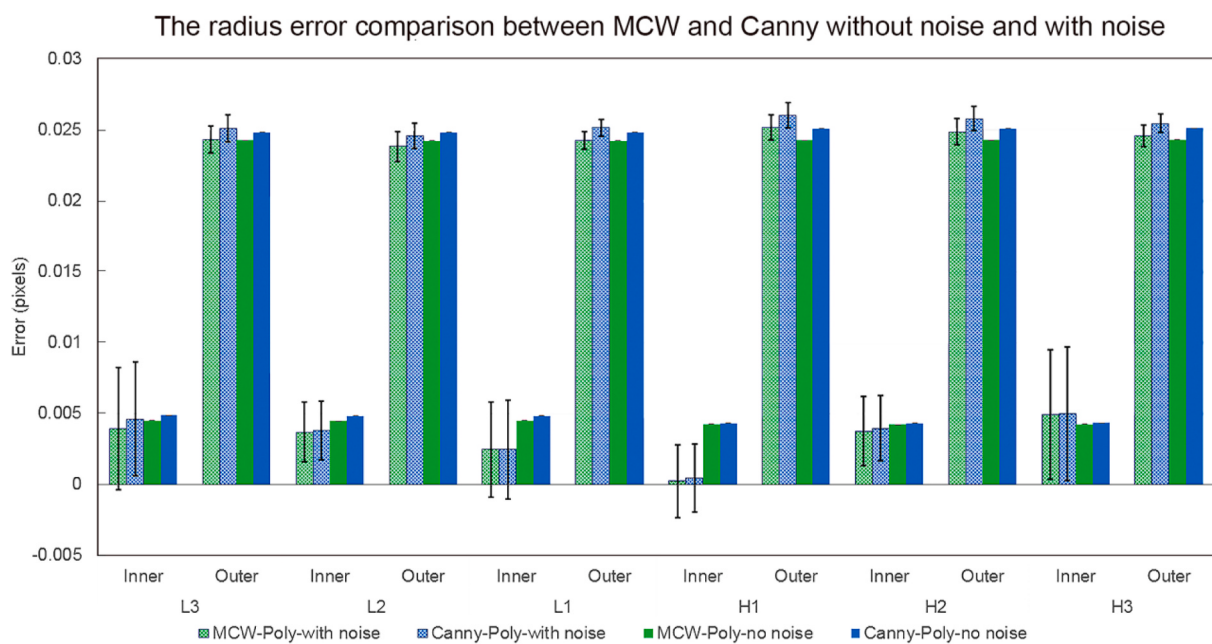


Fig. 16. The radius error result for simulation set 2 ($SNR = \infty$) and simulation set 3 ($SNR = 155$), polychromatic, Interpolation ratio $p = 0.1$, mean radius value and error bars are based on 5 individual MCW and Canny applications over 5 slices within the range of ± 10 layers around each benchmark (L3-H3) layers. Error bars indicate the standard deviation for each radius value.

Whilst the outer diameter measurement results are affected by a larger bias, we observe a better overall measuring accuracy of the inner diameters.

5. Discussions of MCW algorithm parameters

5.1. Influence of marker size and position

According to Fig. 17 A and B, both automatic [48] and manual MCW method generated closed surfaces. Both methods have the following typical results:

- There is only one marker that labels the foreground.
- As the background is divided into two parts by the foreground, two markers label the background.
- Each marker is entirely within the range of the proposed segment: none of the marker intersects with the proposed watershed surface.
- The markers do not contain any gaps.

However, differences in computational time are significant. Table 2 describes the computational time of the MCW algorithm in comparison to the Canny and ISO50 methods. According to Table 2, computing time based on manual selection was six times longer than the automatic selection. Smaller markers resulted in larger areas to assess during the geodesic and watershed transformations, increasing the computing time. Compared with the ISO50 algorithm, which only searches the pixels with the pre-defined single threshold value, the MCW's computation time drastically increased due to multiple image computations: marker generation, interpolation, gradient transformation, geodesic transformation, etc. Also, the Canny algorithm computation time is only half of the automatic watershed. This study is yet to optimise the watershed computation time, and future work is mentioned in conclusion.

5.2. Influence of interpolation ratio

Fig. 18 depicts the voxels surrounding a portion of the outer cylinder surface from which outer cylinder was calculated and the point cloud associated with the cylinder surface at different interpolation ratios. Without interpolation, as $p = 1$, the radius calculations were affected by errors as large as 0.7 of the size of the pixel. For $p = 0.1$, most of the estimated surface points were distributed within a narrow band from the CAD data.

Fig. 19 shows the relationship between the interpolation ratio p and root-mean-square deviation (RMS) value of the residual of the point

Table 2

The comparison of computing time with different marker-selection methods (based on 0.1 interpolation ratio). The processor was Intel Xeon CPU E5-2630 v2 2.60 GHz.

SD algorithms	Computing time (s)
Automatic MCW	32
Manual MCW	193
ISO 50	1
Canny	15

clouds against the fitted circle. Decreasing p value (increasing interpolation ratio) reduces the standard deviation associated with circle fitting.

Fig. 20 presents the mean radius errors and the associated standard deviations for different interpolation ratios and measurement conditions, i.e. with and without noise. The worse results were recorded for $p = 1$, meaning that the bias was significant without interpolation.

Excluding $p = 1$ case, for the inner cylinder, the best results calculated from the data without noise were obtained at $p = 0.2$. In polychromatic case, without noise and $p = 0.2$, the bias of the internal radius measurement did not exceed 0.4% of the pixel size, but the outer cylinder radius bias was as large as 2.5% of pixel size. The radius of the outer diameter was not significantly different for $p = 0.1$ and $p = 0.2$.

According to Fig. 19, increasing interpolation resolution (lower p) can reduce the RMS of point cloud residuals. However, the errors of inner cylinders' radii at $p = 0.1$ for H1, H2 and H3 were larger than the bias recorded at $p = 0.2$ and 0.5. This result shows that the interpolation process can introduce additional errors.

As expected, the standard deviation of the measurement results that include noise effects were found to be larger than the one for the simulations without noise. The standard deviation associated with the inner cylinder measurements was significantly larger than the one associated with outer diameters, suggesting that the interpolation algorithm can cause additional systematic errors.

5.3. Comparison of MCW and Canny algorithm

Fig. 21 shows the comparison of the determined edges that are calculated by automatic MCW and the Canny algorithm. The Canny algorithm implementation can lead to different edge positions, which is also dependent on the selection of the thresholds. The Canny algorithm was run four times before achieving a clean edge for a threshold vector of [0.3 0.4]. [0.05 0.1] threshold led to noisy edges, [0.2 0.9] only detected the outer circle edge, [0.7 0.9] detected half of the outer edge, [0.4 0.5]

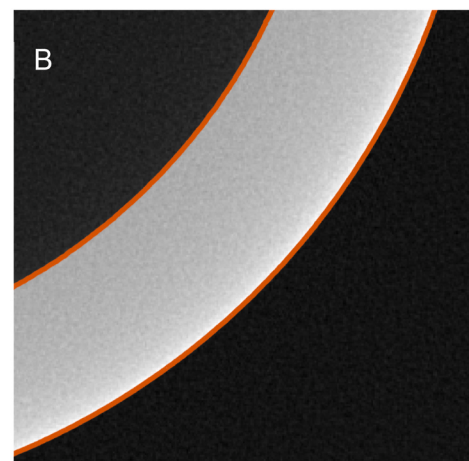
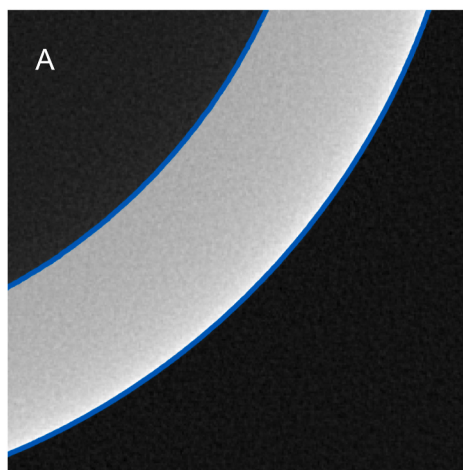


Fig. 17. A. Watershed surface based on the geodesic transformed representation with auto-selected markers; B. Watershed surface based on the geodesic transformed representation with randomly selected marker.

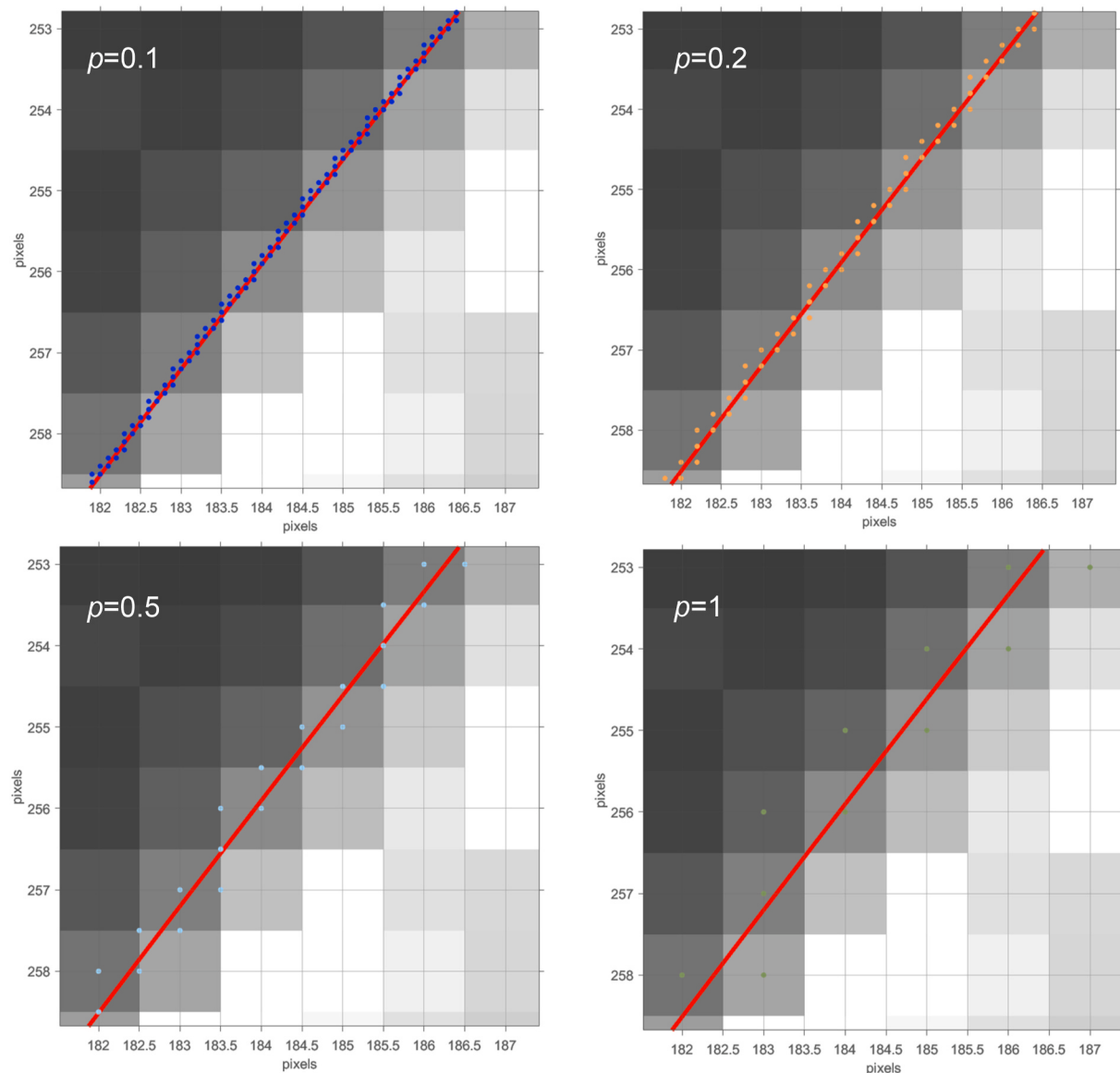


Fig. 18. Surface point clouds determined by MCW under simulation set 2: Polychromatic, no noise. Outer Circle; Slice height index: L2, Interpolation ratio $p = 0.1$ (blue dot), $p = 0.2$ (orange dot), $p = 0.5$ (cyan dot) and $p = 1$ (no interpolation, green dot), red line = nominal circle. (For interpretation of the references to colour in this figure legend, the reader is referred to the Web version of this article.)

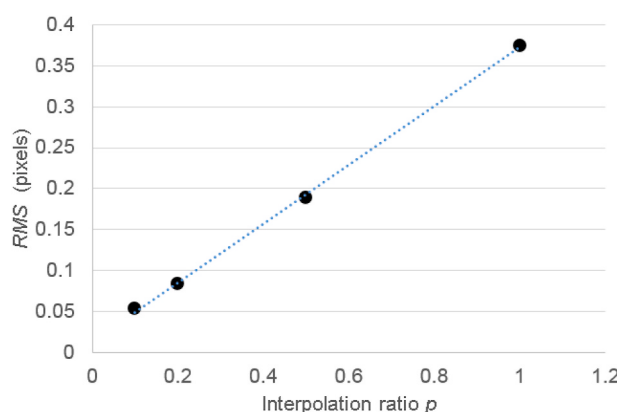


Fig. 19. The scatter plot of the relationship between p and RMS of the residual against fitted circle, Simulation set 2: Polychromatic, without noise.

could establish the outer edge but lead to an intermittent inner circle edge, demonstrating that the selection of *threshold* values significantly impacts the edge result of the Canny algorithm.

In contrast, MCW computed a closed edge within a single trial. The foreground marker and the background marker were selected automatically. The watershed transformation segmented the geodesic transformed gradient image into partitions (material and background) whose edges are strictly closed. The result shows that the MCW can potentially be applied as an automated SD algorithm that does not require an educated input from the operator, hence reducing any associated operator errors.

Despite the issues related to threshold selection in the Canny algorithm, the results presented until this point show that both methods, Canny and MCW provide equivalent results. This is because the surface of the object used in this research resembles an ideal situation, which is rarely met in practice. The difference between the MCW and Canny becomes visible when applied to real measurements of objects that are characterised by complex surface textures as shown in Fig. 22. Compared to the Canny algorithm, which generates disconnected edges

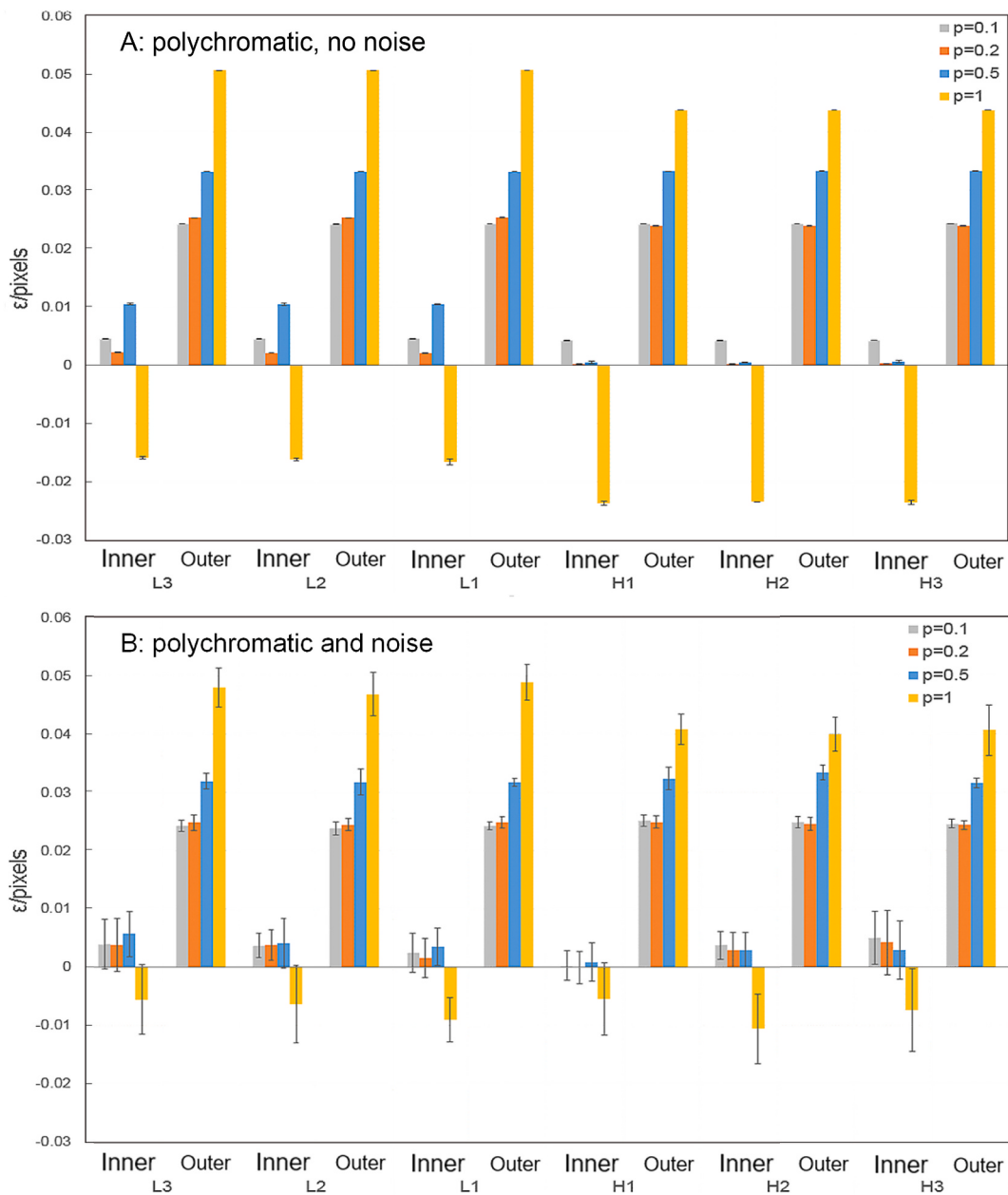


Fig. 20. The radius deviation of fitting circle against the nominal radius value under different interpolation ratio p value: A. Simulation set 2, polychromatic, with noise; B. Simulation set 3, polychromatic, SNR = 155. Mean radius value and error bars are based on five individual watershed surface applications over 5 slices within the range of ± 10 layers around each benchmark (L3-H3) layers. Error bars indicate the standard deviation for each radius value.

nearby severe measuring artefacts, MCW successfully provides only closed edges surrounding the feature of interests.

To conclude our discussions, we also present in Fig. 23 the MCW results applied on the real measurement of the two spheres, introduced in the first section of this paper as an example of 'streak' artefacts effect (see Fig. 2), highlighting once again the MCW resilience to common XCT measurement errors.

6. Conclusions

In summary, it has been identified that SD algorithms play an essential role in XCT measurements [59]. In this paper, we have addressed some of the issues encountered with the SD process: algorithm transparency, operator induced errors and the ability of the SD algorithms to avoid the effect of the noise and beam hardening that can lead to false edges. In order to reduce the operator's errors, an automatic SD

algorithm based on the MCW algorithm that eliminates the over-segmentation issues has been proposed and evaluated for XCT inspection of samples with smooth and rough surfaces. The MCW algorithm consists of four steps: marker selection; gradient transformation; geodesic transformation; watershed transformation. The main points to highlight here are:

- The foreground and background markers are determined automatically by combining the closing and erosion operators. Closing operator eliminates the small hole within the marker to avoid subsequent over-segmentation and erosion shrinks the marker area so that markers do not overlap with the pixels adjacent to the edges.
- The geodesic transformation removes the unwanted regional features present in the gradient image, which can lead to false edges.
- The watershed transformation produced a clean and closed surface without significant errors.

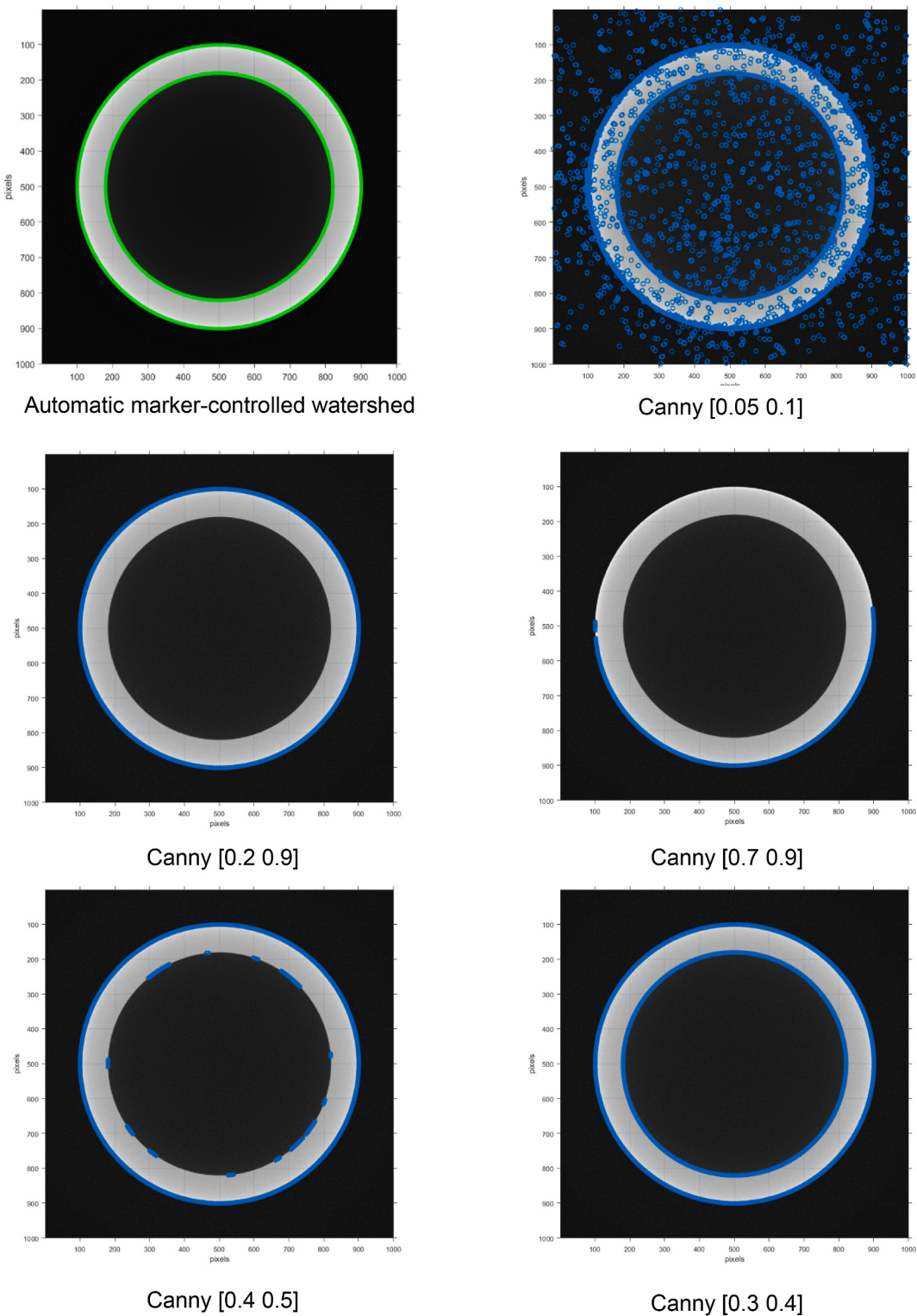


Fig. 21. The edge determined using automatic marker-controlled watershed and Canny algorithm. The number in the square brackets indicate the threshold in the canny edge determination algorithm in MATLAB, and each number is within (0,1). The image is acquired under the CT simulation with noise.

In conclusion, the MCW is an effective SD algorithm that has been successfully validated for XCT metrology and inspection purposes using simulations and a reference sample. Additionally, we found that:

- Compared to the Canny algorithm, the MCW algorithm can effectively provide closed inner and outer edges and avoids the errors attributed to the operator. At the same time, the MCW algorithm is

easier to use compared to the Canny algorithm because it does not need to find the optimal thresholding conditions using ‘trial and error’ tests.

- Both automatic and manual marker selections lead to the same edge data.

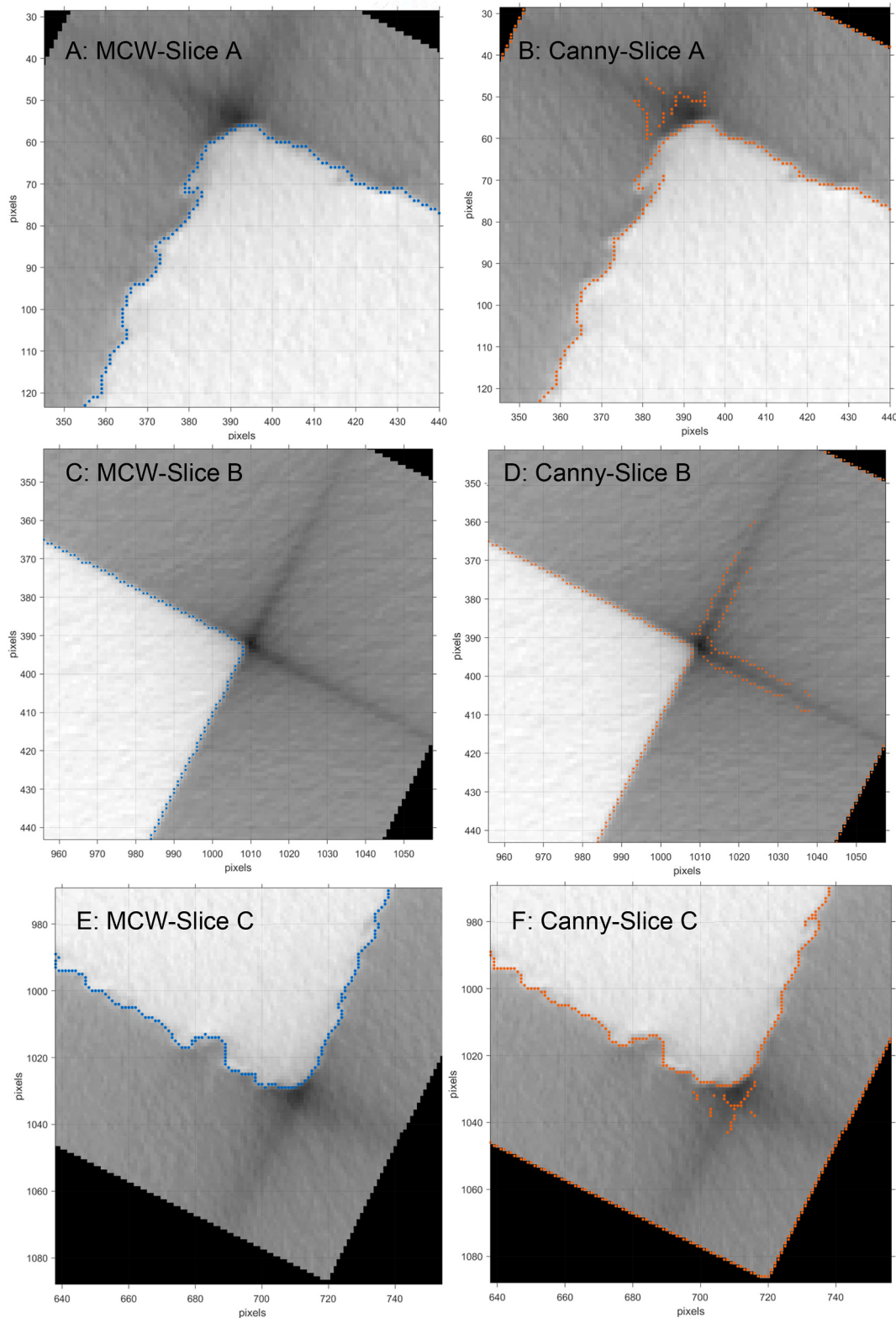


Fig. 22. The comparison between 3D MCW and 3D canny surfaces for surface roughness analysis over the experimental reference sample.

- Interpolation is necessary to achieve sub-pixel (or sub-voxel) surface point clouds, however, there are no significant improvements below $p = 0.2$.
- At $p = 0.2$ and in polychromatic measurement conditions, the radius of the external cylinder is affected by an error that can be as large as 2.5% of a pixel compared to 0.4% in the case of the inner cylinder.

- The noise leads to twice as large residual errors associated with the circle fitting of the external features than the ones reported for the inner features (0.5% and 0.25% of pixel size, respectively).
- The geodesic transformation only eliminates most of the local minima that can lead to false edges.

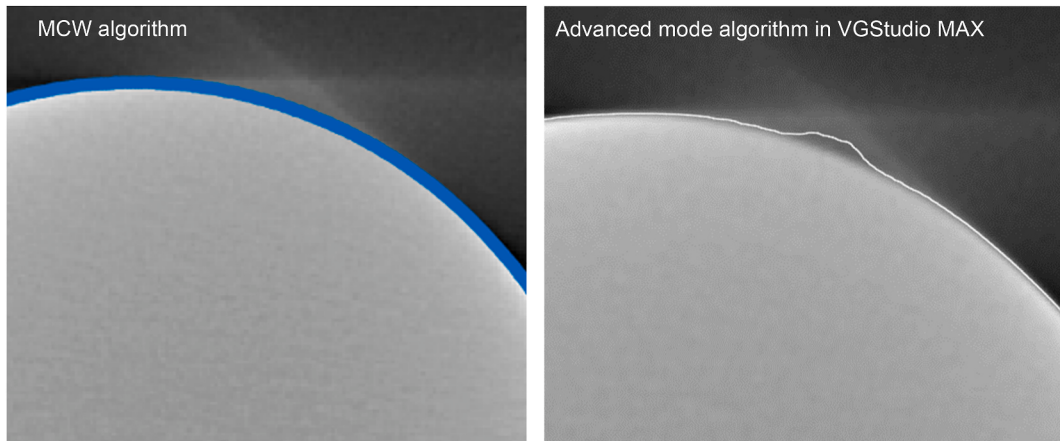


Fig. 23. The comparison between the MCW and ‘advanced mode’ in commercial VGStudio software in dealing with ‘streak’ artefact caused by beam hardening.

- The MCW algorithm outperforms the Canny algorithm when used to determine the surface of measured objects with complex surfaces. Applied on real XCT measurements, MCW generated the closed edges around the feature of interests and the results were not affected by the surrounding measurement artefacts such as in the Canny algorithm case.
- Compared to commercial VG algorithm, MCW demonstrates resilience to common XCT measurement errors such as ‘streak’ artefacts.

This work only considered 2D implementation of MCW. Further application on 3D volume data is possible, but it needs better computational capacity and/or algorithm refinement to decrease the need for computer memory. For example, the 2D interpolation process increases the number of pixels from 2000×2000 to $20,000 \times 20,000$, which requires 3051 MB of CPU memory. In 3D, interpolating the float voxel data from $2000 \times 2000 \times 2000$ to $20,000 \times 20,000 \times 20,000$ requires 59,604.64 GB.

Apart from the computer processing capacity, future work should take into account in depth consideration of the 3D MCW implementation, experimental samples, reducing the processing time, the effect of scattering [53] and on the MCW ability to cope with rough components, such as the ones produced by additive manufacturing [20]. Porosity related measurement with smaller spatial frequency should be validated using MCW. Moreover, the geometry fitting strategy should also be considered.

Data underlying this study can be accessed through the Cranfield University repository (CORD) at: <https://doi.org/10.17862/cranfield.rd.20135006>.

This project contains the following underlying data:

- Data_file.zip (Reconstructed simulation data, MCW surface point clouds, measurement results used for Fig 14 and Fig 16).

Data are available under the terms of the [Creative Commons Attribution 4.0 International (CC BY 4.0)].

Author statement

Xiuyuan Yang: Conceptualization, Methodology, Software, Validation, Investigation, Formal analysis, Writing-Original Draft, Visualization. **Wenjuan Sun:** Writing-Review & Editing, Supervision, Project administration, Funding acquisition, Conceptualization, Methodology. **Claudiu Giusca:** Writing-Review & Editing, Supervision, Funding acquisition, Conceptualization, Methodology.

Declaration of competing interest

The authors declare that they have no known competing financial interests or personal relationships that could have appeared to influence the work reported in this paper.

Acknowledgements

This work was funded by the UK Government’s Department for Business, Energy and Industrial Strategy (BEIS) through the UK’s National Measurement System programmes and Centre for Doctoral Training (CDT) in Ultra Precision at Cranfield University which is supported by the RCUK via Grant No.: EP/K503241/1.

References

- [1] du Plessis A, Yadroitsev I, Yadroitseva I, Le Roux SG. X-ray microcomputed tomography in additive manufacturing: a review of the current technology and applications. *3D Print Addit Manuf* 2018;5(3):227–47.
- [2] Carvalho LE, Sobieranski AC, von Wangenheim A. 3d segmentation algorithms for computerized tomographic imaging: a systematic literature review. *J Digit Imag* 2018;31(6):799–850.
- [3] Sun W, Giusca C, Lou S, Yang X, Chen X, Fry T, Jiang X, Wilson A, Brown S, Boulter H. Establishment of x-ray computed tomography traceability for additively manufactured surface texture evaluation. *Addit Manuf* 2022;50:102558.
- [4] Vdi/vde 2630 blatt 1.2, technische regel, entwurf, 2008-12, computertomografie in der dimensionellen messtechnik - einflussgrößen auf das messergebnis und empfehlungen für dimensionelle computertomografie-messungen. 2008.
- [5] Lifton JJ, Malcolm AA, McBride JW. On the uncertainty of surface determination in x-ray computed tomography for dimensional metrology. *Meas Sci Technol* 2015;26(3):035003.
- [6] Jcgm. Evaluation of measurement data-guide to the expression of uncertainty in measurement évaluation des données de mesure-guide pour l’expression de l’incertitude de mesure. 2008.
- [7] Yagüe-Fabre JA, Ontiveros S, Jiménez R, Chitchian S, Tosello G, Carmignato S. A 3d edge detection technique for surface extraction in computed tomography for dimensional metrology applications. *CIRP Annals* 2013;62(1):531–4.
- [8] Jiménez-Pacheco R, Ontiveros S, Yagüe-Fabre JA. A surface extraction analysis in a multi-material test part for computed tomography in metrology applications. *Procedia Manuf* 2017;13:487–94.
- [9] Canny J. A computational approach to edge detection. *IEEE Trans Pattern Anal Mach Intell* 1986;8(6):679–98.
- [10] Kowalcuk T, Woźniak A. A new threshold selection method for x-ray computed tomography for dimensional metrology. *Precis Eng* 2017;50:449–54.
- [11] MacAulay GD, Senin N, Giusca CL, Leach RK. Comparison of segmentation techniques to determine the geometric parameters of structured surfaces. *Surf Topogr Metrol Prop* 2014;2(4):044004.
- [12] Lifton JJ, Liu T. Evaluation of the standard measurement uncertainty due to the iso50 surface determination method for dimensional computed tomography. *Precis Eng* 2020;61:82–92.
- [13] Gómez HV. Studies of dimensional metrology with x-ray cat scan. The University of North Carolina at Charlotte; 2018.
- [14] Otsu N. A threshold selection method from gray-level histograms. *IEEE Transactions on Systems, Man, and Cybernetics* 1979;9(1):62–6.
- [15] Reinhart C, Weg W. Industrial computer tomography - a universal inspection tool. 2008.

- [16] Hiller J, Hornberger P. Measurement accuracy in x-ray computed tomography metrology: toward a systematic analysis of interference effects in tomographic imaging. *Precis Eng* 2016;45:18–32.
- [17] du Plessis A, Yadroitsev I, Yadroitsev I. Effects of defects on mechanical properties in metal additive manufacturing: a review focusing on x-ray tomography insights. *Mater Des* 2020;187:108385.
- [18] Gobert C, Kudzal A, Sietins J, Mock C, Sun J, McWilliams B. Porosity segmentation in x-ray computed tomography scans of metal additively manufactured specimens with machine learning. *Addit Manuf* 2020;36:101460.
- [19] Lifton J, Liu T. An adaptive thresholding algorithm for porosity measurement of additively manufactured metal test samples via x-ray computed tomography. *Addit Manuf* 2021;39:101899.
- [20] Townsend A, Pagani L, Blunt L, Scott PJ, Jiang XQ. Factors affecting the accuracy of areal surface texture data extraction from x-ray ct. *CIRP Ann - Manuf Technol* 2017;66(1):547–50.
- [21] Sokac M, Budak I, Katic M, Jakovljevic Z, Santosi Z, Vukelic D. Improved surface extraction of multi-material components for single-source industrial x-ray computed tomography. *Measurement* 2020;153:107438.
- [22] Lou S, Pagani L, Zeng W, Jiang X, Scott PJ. Watershed segmentation of topographical features on freeform surfaces and its application to additively manufactured surfaces. *Precis Eng* 2020;63:177–86.
- [23] Leach R, Haitjema H, Su R, Thompson A. Metrological characteristics for the calibration of surface topography measuring instruments: a review. *Meas Sci Technol* 2020;32(3):032001.
- [24] Carmignato S, Aloisi V, Medeossi F, Zanini F, Savio E. Influence of surface roughness on computed tomography dimensional measurements. *CIRP Annals* 2017;66(1):499–502.
- [25] Thompson A, Maskery I, Leach RK, Thompson A, Maskery I, Leach RK. X-ray computed tomography for additive manufacturing: a review. 2016.
- [26] Villarraga-Gómez H. X-ray computed tomography for dimensional measurements. 2016.
- [27] Sun Q, Zheng J, Li C. Improved watershed analysis for segmenting contacting particles of coarse granular soils in volumetric images. *Powder Technol* 2019;356:295–303.
- [28] Villarraga-Gómez H, Herazo EL, Smith ST. X-ray computed tomography: from medical imaging to dimensional metrology. *Precis Eng* 2019;60:544–69.
- [29] Nathanael T. Erosion and dilation of edges in dimensional x-ray computed tomography images. 2020.
- [30] Townsend A, Pagani L, Blunt L, Scott PJ, Jiang X. Factors affecting the accuracy of areal surface texture data extraction from x-ray ct. *CIRP Annals* 2017;66(1):547–50.
- [31] Townsend A, Pagani L, Scott P, Blunt L. Areal surface texture data extraction from x-ray computed tomography reconstructions of metal additively manufactured parts. *Precis Eng* 2017;48:254–64.
- [32] Lifton JJ. The influence of scatter and beam hardening in x-ray computed tomography for dimensional metrology. University of Southampton; 2015.
- [33] Steinbeiß HP. Dimensionelles messen mit mikro-computertomographie. Hieronymus; 2005.
- [34] Fleßner M, Müller A, Helmecke E, Hausotte T. Automated detection of artefacts for computed tomography in dimensional metrology. *Digital Industrial Radiology and Computed Tomography* 2015:1–8.
- [35] Brunke O, Santillan J, Suppes A. Precise 3d dimensional metrology using high-resolution x-ray computed tomography (muct). SPIE. 2010.
- [36] Heinzl C, Kastner J, Georgi B, Lettenbauer H. Comparison of surface detection methods to evaluate cone beam computed tomography data for three dimensional metrology. 2007.
- [37] Heinzl C, Klingsberger R, Kastner J, Gröller ME. Robust surface detection for variance comparison and dimensional measurement. *EuroVis*; 2006. p. 75–82.
- [38] Heinzl C, Kastner J, Gröller E. Reproducible surface extraction for variance comparison in 3d computed tomography. Citeseer: Proc. of the 9th European Conference on Non-Destructive Testing; 2006.
- [39] Perona P, Malik J. Scale-space and edge detection using anisotropic diffusion. *IEEE Trans Pattern Anal Mach Intell* 1990;12(7):629–39.
- [40] Lifton JJ, Malcolm AA, McBride JW. An experimental study on the influence of scatter and beam hardening in x-ray ct for dimensional metrology. *Meas Sci Technol* 2016;27(1):015007.
- [41] Körner L, Lawes S, Bate D, Newton L, Senin N, Leach R. Increasing throughput in x-ray computed tomography measurement of surface topography using sinogram interpolation. *Meas Sci Technol* 2019;30(12):125002.
- [42] Staude A. The influence of data filtering on dimensional measurements with ct. Durban, South Africa: WCNDT 2012; 2012.
- [43] Wieclawek W. 3d marker-controlled watershed for kidney segmentation in clinical ct exams. *Biomed Eng Online* 2018;17(1):26.
- [44] Veta M, Huisman A, Viergever MA, Diest PJV, Pluim JPW. Marker-controlled watershed segmentation of nuclei in h&e stained breast cancer biopsy images. In: 2011 IEEE international symposium on biomedical imaging: from nano to macro; 2011. p. 618–21.
- [45] Kanitkar SS, Thombare ND, Lokhande SS. Detection of lung cancer using marker-controlled watershed transform. In: 2015 international conference on pervasive computing (ICPC); 2015. p. 1–6.
- [46] Mangan AP, Whitaker RT. Partitioning 3d surface meshes using watershed segmentation. *IEEE Trans Visual Comput Graph* 1999;5(4):308–21.
- [47] Beucher S. The watershed transformation applied to image segmentation, Scanning microscopy-supplement-. 1992. 299–299.
- [48] Marker-controlled watershed using matlab. <https://uk.mathworks.com/help/images/ref/edge.html>.
- [49] Siu W, Hung K. Review of image interpolation and super-resolution. In: Proceedings of the 2012 Asia pacific signal and information processing association Annual summit and conference; 2012. p. 1–10.
- [50] Sobel I. An isotropic 3x3 image gradient operator. Presentation at Stanford A.I. Project 2014:1968.
- [51] Meyer F. Topographic distance and watershed lines. *Signal Process* 1994;38(1):113–25.
- [52] Vincent L, Soille P. Watersheds in digital spaces: an efficient algorithm based on immersion simulations. *IEEE Trans Pattern Anal Mach Intell* 1991;13(6):583–98.
- [53] Lifton JJ, Carmignato S. Simulating the influence of scatter and beam hardening in dimensional computed tomography. *Meas Sci Technol* 2017;28(10).
- [54] Wang S. Investigation of x-ray computed tomography for dimensional measurement. 2019.
- [55] Pratt V. Direct least-squares fitting of algebraic surfaces. *ACM SIGGRAPH computer graphics* 1987;21(4):145–52.
- [56] Bellon C, Jaenisch G-R. Artist – analytical rt inspection simulation tool. 2007.
- [57] Feldkamp LA, Davis LC, Kress JW. Practical cone-beam algorithm. *Josa a* 1984;1(6):612–9.
- [58] Tan Y, Kiekens K, Welkenhuyzen F, Kruth J-P, Dewulf W. Beam hardening correction and its influence on the measurement accuracy and repeatability for ct dimensional metrology applications. 2012.
- [59] Kruth JP, Bartscher M, Carmignato S, Schmitt R, De Chiffre L, Weckenmann A. Computed tomography for dimensional metrology. *CIRP Annals* 2011;60(2):821–42.